AMERICAN ACADEMY OF OPHTHALMOLOGY®

What Lies beneath Diabetic Macular Edema: Latent Phenotypic Clustering and Differential Treatment Responses to Intravitreal Therapies

Maria Vittoria Cicinelli, MD,[1,2] *Beatrice Leonardo, MDs,*[1] *Giacomo Maiucci, MDs,*[1] *Giuliano Martino, MDs,*[1] *Makan Ziafati, MD,*[3,4] *Soufiane Bousyf, MD,*[1] *Luisa Frizziero, MD,*[5] *Rosangela Lattanzio, MD,*[1,2] *Edoardo Midena, MD,*[5,6] *Francesco Bandello, MD*[1,2]

Purpose: To identify latent phenotypic subgroups of diabetic macular edema (DME) using artificial intelligence–based OCT metrics and evaluate whether treatment responses to anti-VEGF and dexamethasone (DEX) therapies differ across these phenotypic clusters.

Methods: Retrospective study including 114 eyes (82 patients) with treatment-naïve DME. Quantitative OCT metrics, including intraretinal fluid (IRF) and subretinal fluid volumes, IRF % distribution within central 0–1, 1–3, and 3–6 mm, hyperreflective foci counts, and ellipsoid zone (EZ) % disruption, were analyzed before and after treatment.

Main Outcome Measures: Gaussian finite mixture modeling was used to identify distinct DME subgroups. Changes in visual acuity (VA) and OCT parameters following anti-VEGF or DEX therapy were analyzed using linear and generalized linear mixed-effects models, with false discovery rate correction applied to account for multiple comparisons.

Results: Three phenotypic clusters of DME were identified, each demonstrating distinct structural and functional characteristics: cluster 1 (29%, 95% confidence interval [CI]: 20.0%–38.4%), characterized by localized central IRF (mean 0.34 mm^3, 32% in the 0–1 mm zone), moderate structural damage (EZ disruption: 13%), and better VA (mean logarithm of the minimum angle of resolution [LogMAR] 0.29); cluster 2 (49%, 95% CI: 39.6%–57.9%), with diffuse IRF (60% in the 3–6 mm zone), the highest IRF volume (mean: 3.33 mm^3), significant structural disruption (EZ disruption: 46%), and the poorest VA (mean LogMAR: 0.63); and cluster 3 (22%, 95% CI: 13.9%–31.2%), showing intermediate fluid levels and minimal structural damage (EZ disruption: 0.5%). Anti-VEGF therapy led to the greatest VA improvement in cluster 2 (−31.5%, standard deviation: 28.6). Pairwise contrasts showed no significant VA differences between DEX and anti-VEGF in cluster 1 (−26.6%, 95% CI: −64.7 to 11.6) or in cluster 3 (−12.4%, 95% CI: −58.2 to 33.4), although the direction of effect suggested a trend toward greater improvement with DEX. In contrast, cluster 2 showed a nonsignificant difference favoring anti-VEGF (+25.0%, 95% CI: −4.6 to 54.6). For central subfield thickness, DEX achieved a significantly greater reduction than anti-VEGF in cluster 3 (−20.9%, 95% CI: −37.0 to −4.9) and was also associated with a relative increase in peripheral IRF distribution in cluster 3 (+26.7%, 95% CI: 6.5 to 46.9), supporting phenotype-dependent treatment effects.

Conclusions: Latent heterogeneity in DME presentations may influence treatment responses. Artificial intelligence–derived spectral-domain OCT metrics could support tailored therapeutic approaches to optimize patient outcomes.

Financial Disclosure(s): Proprietary or commercial disclosure may be found in the Footnotes and Disclosures at the end of this article. *Ophthalmology Science 2026;6:100975*

Supplemental material available at www.ophthalmologyscience.org.

Diabetic macular edema (DME) is a leading cause of visual impairment in patients with diabetes, driven by the complex interaction between vascular leakage, inflammation, and neurodegeneration within the retina.[1] Despite the availability of effective treatments such as intravitreal anti-VEGF agents and corticosteroid implants (dexamethasone [DEX] and fluocinolone acetonide), individual responses to therapy remain highly variable, underscoring the heterogeneous nature of DME.[2,3] Addressing this variability is critical for optimizing therapeutic strategies and improving clinical outcomes.

Advances in imaging technologies, particularly spectral-domain OCT (SD-OCT), have facilitated detailed characterization of retinal morphology and fluid distribution, offering insights into the pathophysiology of DME.[4]

https://doi.org/10.1016/j.xops.2025.100975
ISSN 2666-9145/25

Concurrently, the integration of artificial intelligence (AI) and quantitative imaging has enabled precise, automated assessments of key structural metrics, including intraretinal fluid (IRF) and subretinal fluid (SRF) volumes, hyperreflective foci (HRF) counts, and ellipsoid zone (EZ) disruption.[5,6] These quantitative metrics provide a robust framework for identifying disease subtypes and tailoring treatments to individual patients.

Although previous studies have highlighted the utility of SD-OCT in predicting treatment responses in DME, most have focused on single biomarkers, such as the presence of HRF or SRF,[7,8] to assess therapeutic outcomes. Although these approaches have been informative, they do not fully capture the complexity of DME, in which multiple structural and functional features may interact to drive disease progression and response variability.[9] The exploration of latent heterogeneity across these features remains limited.

Model-based clustering approaches, such as Gaussian finite mixture modeling, offer a powerful means to uncover latent subgroups within a population.[10] This statistical technique models each subgroup, or cluster, as a Gaussian distribution defined by its mean, variance, and shape parameters. By leveraging multidimensional data, Gaussian finite mixture modeling can classify individuals into distinct clusters based on shared characteristics, even when underlying relationships between variables are complex or nonlinear. This approach is particularly suited for identifying latent phenotypic subgroups in heterogeneous diseases like DME.

In this study, we employed AI-based quantitative SD-OCT metrics and Gaussian finite mixture modeling to identify latent subgroups of DME. Our primary objective was to evaluate whether treatment responses to anti-VEGF and DEX therapies differ across phenotypic clusters, with a focus on structural and functional outcomes.

Methods

This retrospective cohort study included patients with treatment-naïve DME referred to the Medical Retina Unit of the Department of Ophthalmology, Ospedale San Raffaele (Milan, Italy) between 2013 and 2023. The study adhered to the tenets of the Declaration of Helsinki for research involving human subjects. Written informed consent was waived by the local institutional review board because of the retrospective design of the study.

The inclusion criteria included (1) age >18 years; (2) diagnosis of diabetes mellitus (type 1 or type 2); (3) history of DME, defined by the presence of IRF with or without SRF in the central macula; (4) no history of intravitreal injections or focal/pattern laser treatment prior to baseline; and (5) availability of SD-OCT data before and after treatment. The exclusion criteria were (1) retinal or optic nerve diseases other than diabetic retinopathy (DR) (e.g., retinal vein occlusion, age-related macular degeneration, pseudophakic macular edema, uncontrolled glaucoma); (2) media opacities precluding adequate fundus examination or imaging; (3) intraocular surgery or pan-photocoagulation ≤6 months before the first intravitreal injection. For patients with bilateral DME, both eyes were included if they met all the inclusion criteria.

Demographic data (age, gender) and medical history (duration and type of diabetes mellitus, glycated hemoglobin, self-reported hypertension, and history of major cardiovascular events [acute myocardial infarction, angina, or stroke]) were collected at baseline. Ophthalmologic history included the stage of DR (non-proliferative or proliferative), history of cataract extraction, glaucoma, and duration of DME. Baseline ocular examinations included visual acuity (VA) assessment using decimal charts with refraction correction obtained by autorefractometer, subsequently converted into logarithm of the minimum angle of resolution [LogMAR] values for analysis. Slit lamp biomicroscopy, dilated fundus examination, and SD-OCT imaging using Spectralis HRA (Heidelberg Engineering) were also performed. Spectral-domain OCT imaging was acquired with a 19-line horizontal volumetric raster centered on the fovea, covering a 20° × 15° area. Fluorescein angiography was reviewed when available, using either a nonconfocal camera (Topcon TRC-50IX, Topcon Medical Systems) or a confocal camera (Optos plc). The foveal avascular zone was measured on the earliest fluorescein angiography frame using the system's embedded caliper tool and was used as a proxy for macular ischemia.

All patients underwent intravitreal treatment with either anti-VEGF agents (ranibizumab [Lucentis, Novartis] or aflibercept [Eylea, Bayer]) or DEX implants (Ozurdex, Abbvie); corticosteroids were preferred in selected cases based on patient characteristics, such as a history of recent cardiovascular events, expected poor adherence to monthly injections, or pseudophakia. Follow-up visits were scheduled approximately 1 month after the third monthly loading dose of anti-VEGF or 3 months after a single DEX implant injection, with an allowable variability of ±1 month to account for deviations in follow-up timing observed in routine care.

At follow-up, VA measurement and SD-OCT imaging were repeated using the follow-up mode to ensure scan coregistration with previous acquisitions. Patients with proliferative DR underwent panretinal photocoagulation if they had high-risk characteristics.

Quantitative and Qualitative SD-OCT Analysis

Central subfield thickness (CST) was automatically measured in the central 1-mm ETDRS map using Spectralis software. Disorganization of the retinal inner layers (DRIL) was manually defined as the absence of identifiable boundaries between the ganglion cell, inner plexiform, and inner nuclear layers within the central 1-mm area.

Quantitative AI-based measurements were performed using the CE-certified Ophthal software (Version 1.0.2 − January 3, 2024, Mr. Doc s.r.l.), which employs adversarial generative deep learning networks to automatically identify retinal layers and quantify fluid and structural metrics. This software has been validated in patients with DME.[11]

The metrics derived from volumetric scans included IRF and SRF volumes and the percentage of IRF volume in the central 1-mm circle (IRF 0−1 mm), in the 1−3 mm ring (IRF 1−3 mm), and in the 3−6 mm ring (IRF 3−6 mm). The number of HRF within the central 3-mm diameter region (encompassing both the central 0−1 mm and 1−3 mm zones) and the percentage of external limiting membrane (ELM) and EZ disruptions within the central 1-mm zone were extracted from the foveal scan (Fig 1). These metrics, providing detailed anatomical and structural data for evaluating treatment responses, were computed before and after treatment.

Statistical Analyses

Statistical analyses were conducted using R (R Core Team). Quantitative variables were summarized as mean ± standard deviation (SD) for normally distributed data or as median and

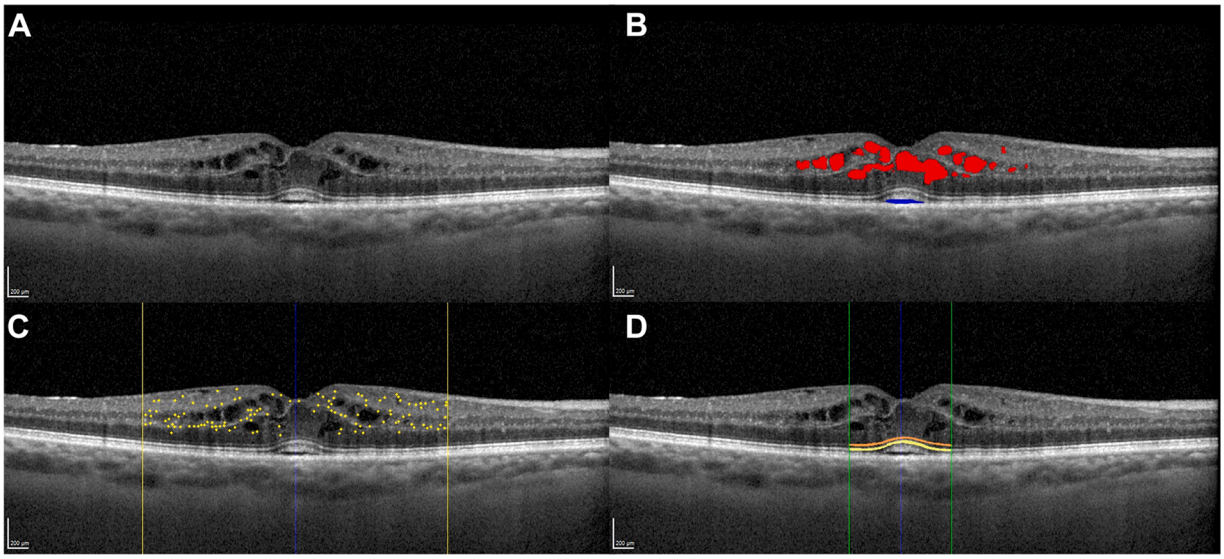

Figure 1. Spectral-domain OCT biomarkers analyzed in the study by artificial intelligence quantification tool (Ophthal). (**A**) Unprocessed SD-OCT image before segmentation. (**B**) Segmentation of intraretinal fluid (red) and subretinal fluid (blue) within the scan. (**C**) Detection of hyperreflective foci (yellow dots) in the central 3-mm region (marked by yellow vertical lines). (**D**) Identification of the external limiting membrane (orange) and ellipsoid zone (yellow) within the central 1-mm region (marked by green lines). This illustration highlights key imaging features used for quantitative analysis. SD-OCT = spectral-domain OCT.

interquartile range for non-normally distributed data. Categorical variables were described as frequencies and percentages.

Pairwise correlations among baseline variables were calculated using Pearson correlation coefficient. A correlation matrix was visualized through scatterplots and histograms to evaluate linear relationships. The same analysis was repeated for posttreatment variables to explore changes in correlations over time.

To identify latent subgroups within the data, model-based clustering was performed using the *Mclust* R package.[12] A subset of baseline variables was selected for clustering to minimize collinearity and ensure model stability. These included IRF volume, IRF % distribution in the central 0−1 mm and 3−6 mm zones (excluding the 1−3 mm zone because of collinearity), SRF volume, HRF count, and EZ % disruption. Variables with skewed distributions, such as SRF volume, were square-root transformed to approximate normality.

A multivariate Gaussian finite mixture model was applied to the scaled data set. The optimal number of clusters (G) was determined by minimizing the Bayesian Information Criterion, which balances model fit against model complexity to avoid overfitting. Models with 1 to 9 clusters across all covariance structures were evaluated, and the best-fitting solution corresponded to a 3-cluster model with variable volume, equal shape, and variable orientation covariance structure. Cluster assignments were visualized in reduced-dimensional space, and the stability of the classification was confirmed using bootstrap resampling via the MclustBootstrap function, which provided confidence intervals (CIs) for cluster membership probabilities.

Cluster assignments were incorporated into the data set as a categorical variable representing the 3 latent subgroups. Differences between clusters were analyzed using linear mixed-effects models for continuous outcomes, with cluster membership as a fixed effect and patient identifier as a random effect. Binary outcomes were evaluated using generalized linear mixed-effects models with a binomial link function. To account for multiple comparisons across the fixed-effect terms from all models, we applied false discovery rate (FDR) correction to the corresponding *P* values.

The primary outcome was to assess whether treatment efficacy differed between drug types (anti-VEGF vs. DEX) and across clusters, while also evaluating potential interactions between these factors. Treatment responses were quantified as percentage changes from baseline for structural and functional metrics initially expressed as absolute values (e.g., VA, CST, IRF volume, HRF count) using the formula:[13]

$$\%\text{Change} = \frac{\text{Value}_{\text{Post-Treatment}} - \text{Value}_{\text{Baseline}}}{\text{Value}_{\text{Baseline}}} \times 100$$

We opted for this approach because linear mixed models with repeated measures, though potentially ideal for longitudinal assessment, were not feasible in our setting. Specifically, modeling VA as a function of time, cluster, and treatment (VA ∼ time * cluster * treatment) would have required estimating a triple interaction with insufficient power and unstable estimates because of limited sample sizes within clusters. For metrics already expressed as percentages (e.g., IRF 0−1 mm, IRF 3−6 mm, EZ disruption), percentage differences were calculated directly. For SRF, absolute changes were used because of the skewed baseline distribution and disproportionately large percentage changes.

Linear models were employed to evaluate the effects of treatment type (anti-VEGF vs. DEX), cluster membership, and their interaction on percentage changes in outcomes. The main effect of treatment type represented the average difference in percentage change between DEX and anti-VEGF within the reference cluster, whereas the main effect of cluster membership indicated differences in percentage change between the reference and other clusters under anti-VEGF treatment. Interaction terms assessed whether the relative efficacy of DEX compared to anti-VEGF varied by cluster, with significant interactions suggesting that treatment responses were influenced by cluster membership. Effect sizes were reported as estimate and standard errors. To mitigate potential bias in percentage change calculations caused by baseline values (e.g., higher percentages associated with better

baseline LogMAR vision), all models were adjusted for baseline values. Pairwise treatment contrasts (DEX vs. anti-VEGF within each cluster) and corresponding 95% CIs were derived using the *emmeans* package.

To control for multiple testing, FDR correction using the Benjamini–Hochberg method was applied separately within each outcome, treating the 3 within-cluster treatment contrasts as a single family of tests. This approach appropriately controls the FDR while avoiding excessive loss of power.

Only FDR-adjusted P values < 0.05 were considered statistically significant.

Results

Study Participants and Clinical Characteristics

This study included 82 participants (mean age: 61.6 ± 12 years, range: 20–83 years), 60% of whom were male. The majority (89.5%) had type 2 diabetes mellitus, with an average disease duration of 16 years (range: 5 months–50 years). Hypertension was present in 53.5%, and 19.3% reported a history of cardiovascular events. Glycemic control, measured by glycated hemoglobin, averaged 7.64% (range: 5.10%–11.6%).

A total of 114 eyes were analyzed. Nonproliferative DR was observed in 78% of eyes, with a mean DME duration of 4 months (median: 0.5 months, range: 0–34 months). Baseline VA was 0.46 ± 0.37 LogMAR (range: 0–1.20), and CST averaged 495 ± 119 μm (range: 282–904 μm). Imaging metrics revealed DRIL in 32% of eyes, ELM disruption of 19 ± 30%, EZ disruption of 27 ± 35%, and SRF in 43% of eyes (Table 1).

Correlation Analysis

Baseline correlations highlighted relationships between structural metrics, fluid distribution, and visual function. A significant negative correlation between log-transformed DME duration and CST ($r = -0.32$, $P < 0.001$) suggested a reduction in retinal thickness with longer disease duration, potentially reflecting chronic atrophic changes. Similarly, SRF volume negatively correlated with DME duration ($r = -0.29$, $P = 0.002$), indicating SRF as an earlier disease manifestation.

Visual acuity showed a nonsignificant positive association with CST ($r = 0.18$, $P = 0.05$) and was better when IRF was confined to the central macula (IRF 0–1 mm: $r = -0.32$, $P < 0.001$). Conversely, extrafoveal fluid correlated with worse VA (IRF 3–6 mm: $r = 0.32$, $P < 0.001$). Visual acuity showed no significant correlation with SRF volume ($r = 0.07$, $P = 0.48$).

Central subfield thickness was higher with diffusely distributed fluid (negative correlations with IRF 0–1 mm: $r = -0.23$, $P = 0.014$; IRF 1–3 mm: $r = -0.24$, $P = 0.01$). Subretinal fluid correlated positively with peripheral IRF in the 3-6 mm zone ($r = 0.33$, $P < 0.001$), reflecting SRF is more prominent with predominant extrafoveal fluid distribution.

Disruptions in ELM and EZ were strongly associated with both higher CST and worse VA ($P < 0.001$), indicating their role as markers of advanced structural damage. Hyperreflective foci counts showed weak associations with VA ($r = 0.19$, $P = 0.04$) but no significant correlation with CST or fluid metrics, suggesting an independent role (Supplementary Fig 1A, available at www.ophthalmologyscience.org).

Posttreatment Correlations

Posttreatment, the factors associated with retinal morphology and visual outcomes shifted. The baseline correlation between VA and CST was no longer present ($r = 0.03$, $P = 0.75$). Intraretinal fluid volume correlated with persistent SRF ($r = 0.36$, $P < 0.001$), reflecting recalcitrant disease activity. Weakening correlations between CST and ELM/EZ disruptions suggest these disruptions primarily reflect pre-existing damage rather than fluid-driven changes (Supplementary Fig 1B, available at www.ophthalmologyscience.org).

Gaussian Mixture Modeling

Artificial intelligence–derived metrics revealed significant latent heterogeneity in DME features across the 114 eyes included in the analysis. For IRF volume, 2 clusters were identified: a low-volume group (mean: 0.41 mm^3 [SD 0.27], 37% of eyes) and a high-volume group (mean: 2.96 mm^3 [SD 1.64], 63% of eyes). Fluid centralization was analyzed, with IRF in the 0–1 mm zone forming 3 clusters (means: 5% in 45% of eyes, 18% in 41% of eyes, and 46% in 14% of eyes), reflecting varying degrees of central involvement. Intraretinal fluid distribution in the 3–6 mm zone revealed 2 clusters (means: 18% in 41% of eyes and 62% in 59% of eyes), indicating a spectrum of peripheral fluid accumulation. Subretinal fluid volume formed 2 distinct clusters: minimal SRF (mean: 0.09 mm^3 [SD 0.16], 92% of eyes) and elevated SRF (mean: 1.06 mm^3 [SD 0.16], 8% of eyes). Hyperreflective foci count and EZ disruption also clustered distinctly, with the majority of eyes exhibiting low HRF counts (mean: 91 lesions [SD 39.5], 97% of eyes) and minimal EZ disruption (mean: 3%, 45% of eyes). However, a subset exhibited severe EZ disruption (mean: 96%, 15% of eyes) (Supplementary Table 1, Supplementary Fig 2, available at www.ophthalmologyscience.org).

When metrics were combined in a multivariable Gaussian finite mixture model using the VEV structure, 3 distinct clusters were identified (Supplementary Fig 3, available at www.ophthalmologyscience.org): cluster 1 (29%, 95% CI: 20.0%–38.4%) characterized by low variance and a homogenous phenotype; cluster 2 (49%, 95% CI: 39.6%–57.9%) marked by high variance between IRF, SRF, and EZ disruption; and cluster 3 (22%, 95% CI: 13.9%–31.2%) with weaker covariances, reflecting more independent contributions of fluid and structural metrics (Fig 2 and Supplementary Fig 4, available at www.ophthalmologyscience.org).

Cluster Characteristics

The 3 clusters demonstrated distinct clinical, demographic, and imaging characteristics, reflecting different severities and patterns of DME (Table 1). Estimates represent

Table 1. Eye-Level Baseline Characteristics across 3 Identified Clusters, Including Demographic Data, Diabetes-Related Metrics, Ocular Parameters, and Imaging Features

Variable	Cluster 1 (N = 33 Eyes)	Cluster 2 (N = 56 Eyes)	Cluster 3 (N = 25 Eyes)	Overall (N = 114 Eyes)
Age (years)	65.0 (8.82)	59.9 (11.3)	60.7 (16.2)	61.6 (12.0)
Male gender	18 (54.5%)	30 (53.6%)	20 (80.0%)	68 (59.6%)
Type 2 diabetes	27 (81.8%)	53 (94.6%)	22 (88.0%)	102 (89.5%)
Diabetes duration (months)	269 (145)	139 (102)	208 (141)	191 (136)
Hypertension	15 (45.5%)	32 (57.1%)	14 (56.0%)	61 (53.5%)
CV events	7 (21.2%)	11 (19.6%)	4 (16.0%)	22 (19.3%)
Pseudophakia	12 (36.4%)	22 (39.3%)	8 (32.0%)	42 (36.8%)
Glaucoma	3 (9.1%)	6 (10.7%)	2 (8.0%)	11 (9.6%)
HbA1c (%)	7.21 (0.978)	7.87 (1.64)	7.71 (1.42)	7.64 (1.44)
DR type				
NPDR	28 (84.8%)	40 (71.4%)	21 (84.0%)	89 (78.1%)
PDR	5 (15.2%)	16 (28.6%)	4 (16.0%)	25 (21.9%)
DME duration (months)	4.55 (5.18)	2.73 (5.41)	6.74 (9.73)	4.09 (6.59)
VA (LogMAR)	0.290 (0.266)	0.627 (0.385)	0.320 (0.285)	0.462 (0.369)
CST (μm)	425 (73.9)	563 (121)	436 (69.5)	495 (119)
IRF volume (mm^3)	0.337 (0.250)	3.33 (1.60)	1.25 (0.904)	2.01 (1.80)
IRF distribution in central 0−1 mm (%)	31.5 (20.8)	7.18 (5.31)	13.8 (8.66)	15.7 (16.2)
IRF distribution in central 1−3 mm (%)	53.5 (19.4)	33.1 (11.7)	38.2 (14.0)	40.1 (17.1)
IRF distribution in central 3−6 mm (%)	15.1 (13.5)	59.7 (16.4)	48.0 (20.9)	44.2 (25.4)
SRF presence	9 (27.3%)	37 (66.1%)	3 (12.0%)	49 (43.0%)
SRF volume (mm^3)	0.006 (0.015)	0.245 (0.487)	0.0006 (0.002)	0.122 (0.360)
HRF count (lesions)	95.1 (41.8)	102 (60.8)	87.5 (20.5)	96.7 (49.2)
ELM disruption (%)	4.24 (11.5)	35.8 (34.6)	0.840 (4.20)	19.0 (30.0)
EZ disruption (%)	13.1 (18.6)	46.0 (38.1)	0.520 (1.48)	26.5 (34.6)
DRIL	3 (9.1%)	27 (48.2%)	6 (24.0%)	36 (31.6%)
FAZ area (mm^2)				
Nonconfocal camera	0.324 (0.160)	0.447 (0.200)	0.637 (0.370)	0.473 (0.279)
Confocal camera	0.211 (0.089)	0.257 (0.211)	0.177 (0.080)	0.227 (0.162)

CST = central subfield thickness; CV = cardiovascular events; DME = diabetic macular edema; DR = diabetic retinopathy; DRIL = disorganization of the retinal inner layers; ELM = external limiting membrane; EZ = ellipsoid zone; FAZ = foveal avascular zone; HbA1c = glycated hemoglobin; HRF = hyperreflective foci; IRF = intraretinal fluid; LogMAR = logarithm of the minimum angle of resolution; NPDR = nonproliferative diabetic retinopathy; PDR = proliferative diabetic retinopathy; SD = standard deviation; SRF = subretinal fluid; VA = visual acuity.
Values are presented as mean (SD) for continuous variables or counts (percentages) for categorical variables.

differences from the reference cluster with corresponding raw and FDR-adjusted *P* values provided in Supplementary Table 2, available at www.ophthalmologyscience.org. Although age, gender, lens status, history of glaucoma, and type 2 diabetes prevalence were similar across clusters, hypertension was more common in cluster 2 (57%).

Imaging metrics varied significantly among clusters. Cluster 2 exhibited the worst VA (0.627 LogMAR) and the thickest CST (563 μm), consistent with severe DME. Cluster 1 demonstrated better VA (0.290 LogMAR) and thinner CST (425 μm), whereas cluster 3 showed intermediate values. Intraretinal fluid volume was highest in cluster 2 (3.33 mm^3), with fluid predominantly distributed peripherally in the 3−6 mm zone (60%) (Fig 2). In contrast, cluster 1 had the lowest IRF volume (0.34 mm^3), with fluid concentrated in the central 0−1 mm zone (32%).

Subretinal fluid volume and presence also varied across clusters, with cluster 2 having the highest SRF presence (66%) and volume (0.25 mm^3) compared to minimal SRF in clusters 1 (27%) and 3 (12%). Structural damage was most severe in cluster 2, with higher rates of DRIL (48%), ELM disruption (36%), and EZ disruption (46%). Cluster 1 exhibited moderate structural damage (ELM: 4.2%, EZ: 13%), whereas cluster 3 displayed minimal disruptions (ELM: 0.8%, EZ: 0.5%). Notably, the foveal avascular zone area was similar across clusters.

Treatment Outcomes

Anti-VEGF therapy was the predominant treatment across clusters, administered to 61% of cluster 1, 64% of cluster 2%, and 64% of cluster 3, whereas 39%−36% received DEX implants (P=0.8). No significant differences were seen in treatment allocation in terms of demographics and clinical characteristics (Supplementary Table 3, available at www.ophthalmologyscience.org).

Relevant improvements were observed in clinical and imaging metrics posttreatment. Visual acuity improved by 0.10 LogMAR (relative change −17%), CST decreased by 116.4 μm (relative change −22%), and IRF volume reduced by 0.90 mm^3 (relative change −45%). Subretinal fluid volume exhibited the largest proportional improvement, with a reduction of 0.10 mm^3 (relative change −79%). Structural improvements included reduced HRF counts (relative change −10.6%) and ELM disruption (−6.6%).

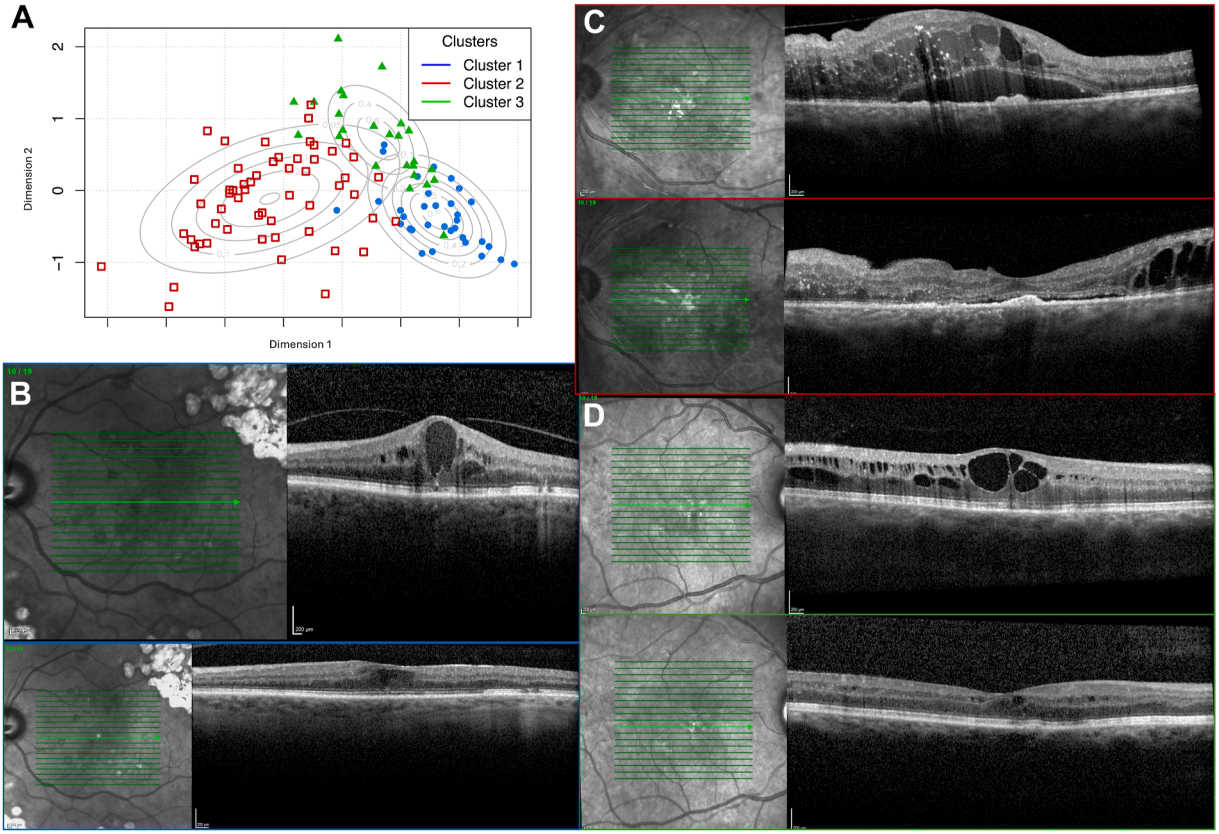

Figure 2. Representative plot and SD-OCT images of the 3 identified clusters before and after treatment, illustrating cluster-specific structural changes in response to therapy. (**A**) Decision boundaries of the latent clusters identified by multivariable Gaussian finite mixture modeling in reduced-dimensional space. The plot visualizes 3 clusters (Cluster 1, Cluster 2, and Cluster 3) along the first 2 discriminant dimensions (Dimension 1 and Dimension 2) derived from dimension reduction of the multivariable model. Each region is color-coded to represent a specific cluster, with contours indicating decision boundaries based on the probabilistic model. Cluster 2, shown occupying the central region, represents the largest subgroup, whereas Clusters 1 and 3 are smaller but distinct. Overlap at the boundaries suggests transitional cases or shared characteristics between clusters. (**B**) Cluster 1: patient treated with a single DEX implant. Baseline SD-OCT shows localized central IRF with no SRF and moderate EZ disruption subfoveally. Posttreatment SD-OCT demonstrates marked reduction in IRF and restoration of retinal architecture. (**C**) Cluster 2: patient treated with 3 monthly anti-VEGF injections. Baseline SD-OCT reveals widespread IRF and SRF with significant retinal thickening and diffuse EZ loss. Posttreatment SD-OCT shows substantial fluid reduction and improved retinal contour. (**D**) Cluster 3: patient treated with a single DEX implant. Baseline SD-OCT indicates intermediate IRF levels, mostly in the central 1−3 mm, with moderate retinal disruption. Posttreatment SD-OCT demonstrates fluid redistribution, with central fluid reduction. DEX = dexamethasone; EZ = ellipsoid zone; IRF = intraretinal fluid; SD-OCT = spectral-domain OCT; SRF = subretinal fluid.

Ellipsoid zone disruption remained basically unchanged (+1.3%). Fluid redistribution was minimal in the central 0−1 mm zone (+0.02%) and the peripheral 3−6 mm zone (+3.2%) but was slightly more relevant in the 1−3 mm zone (−5.8%) (Table 2).

Treatment Outcomes According to Cluster

The analysis of treatment outcomes revealed cluster-specific differences in response to anti-VEGF and DEX therapies across functional and anatomical parameters (raw descriptive percentage changes are reported in Supplementary Table 4, whereas Supplementary Table 5, available at www.ophthalmologyscience.org presents both the estimated differences between groups and the model-based treatment contrasts derived with *emmeans*).

Visual acuity improved most under anti-VEGF therapy in cluster 2, with a mean percentage change of −31.5% (SD 28.6) (Fig 3A). Visual acuity gains under anti-VEGF were smaller in clusters 1 and 3.

Pairwise contrasts showed no significant VA differences between DEX and anti-VEGF in cluster 1 (−26.6%, 95% CI −64.7 to 11.6) or in cluster 3 (−12.4%, 95% CI −58.2 to 33.4), although the direction of effect suggested a trend toward greater improvement with DEX, whereas in cluster 2, a nonsignificant difference was observed in the opposite direction, indicating greater improvement with anti-VEGF (+25.0%, 95% CI −4.6 to 54.6).

Central subfield thickness decreased under anti-VEGF across all clusters, with the largest reduction observed in cluster 2 (−32.5%, SD 24.2, Fig 3B). Pairwise contrasts showed that, compared with anti-VEGF, DEX achieved a significantly greater CST reduction in cluster 3 (−20.9%, 95% CI −37.0 to −4.9, adjusted $P = 0.03$), whereas it was less effective in cluster 2 (+12.8%, 95% CI 2.0 to 23.6, adjusted $P = 0.03$), In terms of fluid distribution, pairwise

Table 2. Cohort-Wide Baseline and Posttreatment Mean Values (±standard deviation), Absolute Changes (±SD), and Relative Percentage Changes (±SD) for Visual and Anatomical Metrics in Patients with DME

Variable	Mean Baseline Value	Mean Posttreatment Value	Absolute Change	Relative Change
VA (LogMAR)	0.46 [0.37]	0.36 [0.32]	−0.10 [0.19]	−16.9% [53.3]
CST (μm)	495.04 [119]	378.6 [121.5]	−116.4 [119.5]	−22% [21]
IRF volume (mm^3)	2.00 [1.80]	1.10 [1.60]	−0.90 [1.35]	−45.1% [85.0]
IRF distribution in central 0−1 mm (%)	15.7 [16.2]	15.7 [16.0]	0.02 [17.1]	NA
IRF distribution in central 1−3 mm (%)	40.1 [17.1]	34.3 [21.5]	−5.83 [22.2]	NA
IRF distribution in central 3−6 mm (%)	44.2 [25.4]	47.4 [31.4]	3.18 [24.6]	NA
SRF volume (mm^3)	0.12 [0.36]	0.03 [0.08]	−0.10 [0.32]	−79.3% [38.2]
HRF count	96.66 [49.2]	86.4 [42.0]	−10.3 [55.2]	−21.4% [135/8]
ELM disruption (%)	18.98 [30.0]	12.4 [26.8]	−6.56 [28.6]	NA
EZ disruption (%)	26.52 [34.6]	27.9 [40.1]	1.32 [35.5]	NA

CST = central subfield thickness; ELM = external limiting membrane; EZ = ellipsoid zone; HRF = hyperreflective foci; IRF = intraretinal fluid; LogMAR = logarithm of the minimum angle of resolution; NA = not applicable; SRF = subretinal fluid; VA = visual acuity.
Metrics include visual acuity, LogMAR, central subfield thickness, intraretinal fluid and subretinal fluid volumes, distribution of IRF volume across the ETDRS zones (0−1 mm, 1−3 mm, and 3−6 mm), hyperreflective foci counts, and disruptions of the external limiting membrane and ellipsoid zone.

contrasts showed that, compared with anti-VEGF, DEX was associated with a significant relative increase in peripheral IRF in cluster 3 (+26.7%, 95% CI 6.5 to 46.9, adjusted $P = 0.04$) (Fig 3C−F). Structural parameters, including HRF counts and EZ disruption, showed minimal changes with either treatment, suggesting these features may represent chronic damage less responsive to pharmacologic intervention (Fig 3G−H).

Discussion

This study underscores the latent heterogeneity in DME presentations and their significant influence on treatment responses. By utilizing advanced clustering techniques and AI-derived SD-OCT metrics, we identified 3 distinct phenotypic subgroups, each characterized by specific structural features and exhibiting differential responses to treatment. These findings reinforce the potential for tailored therapeutic approaches to optimize patient outcomes.

The pathogenesis of DME involves complex retinal interactions, with the integrity of the blood−retinal barrier (BRB) playing a central role. VEGF disrupts the inner BRB by impairing vesicular pathways and intercellular adhesions,[14] whereas anti-VEGF therapies counteract this disruption, restoring fluid transport out of the retina. However, BRB dysfunction extends beyond VEGF-driven pathways, encompassing pericyte loss, glial contributions, and Müller cell dysregulation. Pericyte loss, an early diabetic complication, compromises BRB stability and

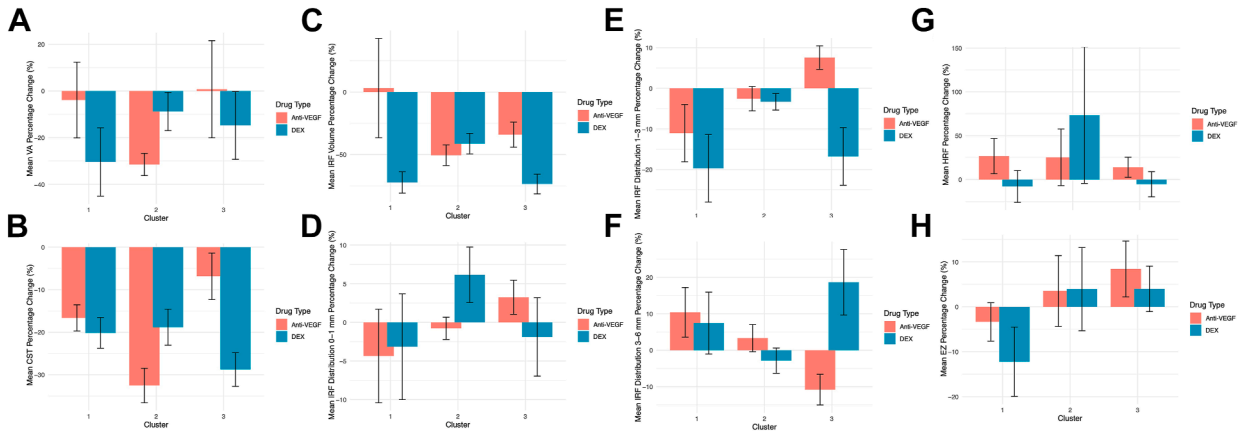

Figure 3. Comparative analysis of treatment responses across clusters and drug types, each panel represents a structural or functional metric's mean percentage change after treatment, grouped by cluster (1, 2, and 3) and drug type (anti-VEGF or DEX), with error bars indicating standard errors. (**A**) The mean percentage change in VA shows the greatest improvement in Cluster 2 with anti-VEGF and Clusters 1 and 3 with DEX. (**B**) Central subfield thickness percentage change demonstrates significant reductions in Cluster 2 with anti-VEGF and Clusters 1 and 3 with DEX. (**C**) Intraretinal fluid volume percentage change highlights prominent reductions in Cluster 2 with anti-VEGF and in Cluster 1 with DEX. (**D**−**F**) Changes in IRF distribution across ETDRS regions (0−1 mm, 1−3 mm, and 3−6 mm) reveal fluid redistribution patterns, with DEX showing central reductions and peripheral shifts in Cluster 3. (**G**) Hyperreflective foci count percentage change shows minimal differences between drug types and clusters. (**H**) Ellipsoid zone disruption percentage change exhibits limited structural improvements, reflecting persistent disruption regardless of treatment type. CST = central subfield thickness; DEX = dexamethasone; EZ = ellipsoid zone; HRF = hyperreflective foci; IRF = intraretinal fluid; VA = visual acuity.

sensitizes endothelial cells to pathological VEGF responses.[15] Müller cells, critical regulators of retinal fluid homeostasis, are disrupted in diabetes because of aquaporin 4 channel dysfunction and inflammation.[16,17] Persistent inflammation exacerbates edema, and emerging mediators, such as angiopoietins 1 and 2, represent additional potential dual-inhibition targets.[18] Artificial intelligence–based imaging analysis offers a powerful tool to enhance understanding of these mechanisms by providing precise localization and quantification of fluid distribution.[6]

A study by Michl et al[13] demonstrated that fluid resolution in DME occurs more slowly and less completely compared to neovascular age-related macular degeneration and retinal vein occlusion, with only 37% of DME cases achieving IRF resolution 1 month after anti-VEGF therapy initiation. These findings reflect the multifactorial pathogenesis of DME, encompassing both VEGF-dependent and independent mechanisms. However, the study did not analyze specific DME phenotypes associated with differential treatment responses, underscoring the need for further research. In our study, the identified clusters revealed clear phenotypic distinctions. Cluster 1, characterized by localized central IRF, minimal SRF, and moderate EZ disruption, represented a less severe phenotype. Cluster 2, the most severe, exhibited diffuse fluid distribution, substantial structural damage, and high SRF volume. Cluster 3 displayed intermediate IRF and SRF volumes with minimal EZ disruption, reflecting relatively preserved retinal structure. One particularly notable finding, which further underscores the complexity of DME and the distinct origins of these clusters, is the independence of the clustering from DME duration. This independence provides an additional layer of evidence for the heterogeneous nature of DME, reinforcing the need to explore pathogenetic mechanisms and their implications for targeted therapeutic strategies in DME management.

Cluster 2 responded most favorably to anti-VEGF therapy, with significant improvements in VA, CST, and IRF volume. In contrast, clusters 1 and 3 responded better to DEX, achieving greater reductions in CST and IRF volume alongside improved VA. Notably, DEX therapy resulted in distinct peripheral fluid redistribution in cluster 3, suggesting a unique mechanism of action that may benefit cases with central fluid involvement. Traditionally, clinical strategies for DME have relied on an initial trial with anti-VEGF agents, followed by an early switch to corticosteroids for poor responders.[19,20] Artificial intelligence may provide an opportunity to refine this decision-making process by identifying the most effective therapeutic agent for each patient, potentially reducing delays and improving outcomes.

Our findings align with prior evidence demonstrating a moderate correlation between VA, CST, and pathological fluid volumes in DME, both at baseline and during the maintenance period.[21] We observed a weak baseline correlation between CST and VA ($r = 0.18$), highlighting the inadequacy of CST alone in explaining VA variability.[22] Posttreatment, the linear correlation between VA and CST was nearly null, as both excessively thick and thin retinas were associated with poor visual outcomes.[23,24] Visual acuity showed a stronger correlation with IRF volume ($r = 0.35$) but this association remained moderate, underscoring the importance of additional biomarkers. Ellipsoid zone disruption, on the contrary, demonstrated the strongest correlation with VA ($r = 0.50$), emphasizing its critical role in visual function, and showed minimal improvement with either therapy.[25] These findings reinforce the importance of early intervention to prevent long-term structural compromise and the limitations of current therapies in reversing advanced damage.

Subretinal fluid has been widely regarded as a biomarker in DME. Consistent with findings from Protocol T[6] and the RESTORE/RESTORE-extension studies,[26] SRF was associated with higher IRF volume at baseline and after anti-VEGF therapy. Patients presenting with SRF had worse baseline vision; however, no direct correlation between VA and SRF volume was identified, aligning with previous reports.[26] Similar to the RESTORE trial, cluster 2 in our study was distinguished by high SRF volume, and these patients responded well to anti-VEGF therapy, showing significant VA gains. These results suggest that SRF, although indicative of a more severe phenotype, may also predict favorable visual recovery with anti-VEGF treatment.

Few studies have investigated the role of cyst characteristics in DME, despite their inclusion in several morphologic classifications.[27] An older study evaluating the efficacy of intravitreal triamcinolone acetonide (IVTA) in DME identified 3 subtypes based on OCT patterns. Sponge-like diffuse retinal thickening, the most common form of DME, was characterized by generalized thickening because of increased vascular permeability, with IVTA showing intermediate effectiveness in reducing CST and improving vision. Cystoid macular edema, characterized by central cystoid spaces within the retina, responded most favorably to IVTA, with a 41% reduction in CST and significant improvement in VA (−0.32 LogMAR). Serous retinal detachment showed limited responsiveness to IVTA, with only a 23% reduction in CST and persistent SRF in most cases.[28] As central cystoid edema is thought to result from Müller cell dysfunction,[29] targeted anti-inflammatory therapy offers a promising approach its management and improving retinal homeostasis.[17] Further research is needed to evaluate how specific cyst patterns can guide modern therapeutic approaches and optimize outcomes.

Although DRIL was suggestive of macular ischemia and disrupted neuronal pathways in DME[30] its prevalence was higher in cluster 2, no significant differences were observed in foveal avascular zone area within our available data. However, splitting the analysis based on confocal and nonconfocal camera acquisition reduced the statistical power. Prospective studies, including those utilizing OCT angiography, are warranted to further investigate associations between clusters and macular ischemia.

Despite notable strengths, our study has limitations. The retrospective design may introduce selection bias, and the relatively small sample size within each cluster limits

generalizability. However, to mitigate selection bias, we included only treatment-naïve eyes with DME, ensuring that clustering was based exclusively on pretreatment structural features rather than on physician-driven treatment choices or posttreatment changes. Correlations between structure and function (e.g., CST and VA) weakened after treatment, highlighting the need to analyze baseline data. Although treatment allocation was similar across clusters, the possibility of physician preference influencing therapy choice cannot be entirely excluded. Additionally, our reliance on SD-OCT metrics, although robust, excludes other potential biomarkers, such as systemic inflammatory markers or peripheral perfusion status.

Although the AI system used in this study is validated, it does not identify fluid location within specific retinal layers, which may have different implications for disease severity and prognosis. For instance, fluid in the inner retina (e.g., inner nuclear layer or ganglion cell layer) may signify more severe retinal damage and a worse functional prognosis.[31] An additional limitation relates to the OCT scan protocol, which used 19 horizontal B-scans over the macular area. Although this pattern was sufficient for capturing key structural features and has been validated in prior studies, it provides lower spatial sampling than denser scan protocols.[32] Finally, this was an exploratory study, and our findings require confirmation in future prospective trials in which patients are randomly assigned to DEX or anti-VEGF therapy within each cluster to validate phenotype-specific treatment responses.

In conclusion, this study underscores the value of phenotype-driven treatment selection in DME and highlights the potential for AI-assisted tools to enhance clinical decision-making, paving the way for more effective and individualized patient care.

Declaration of Generative AI and AI-Assisted Technologies in the Writing Process

During the preparation of this work, the authors used chatGPT4.0 to improve readability and language of the manuscript. After using this tool/service, the authors reviewed and edited the content as needed and took full responsibility for the content of the publication.

Footnotes and Disclosures

Originally received: April 12, 2025.
Final revision: September 22, 2025.
Accepted: October 7, 2025.
Available online: October 14, 2025. Manuscript no. XOPS-D-25-00240.

[1] School of Medicine, Vita-Salute San Raffaele University, Milan, Italy.

[2] Department of Ophthalmology, IRCCS San Raffaele Scientific Institute, Milan, Italy.

[3] Iranian Research Center for HIV/AIDS, Iranian Institute for Reduction of High-Risk Behaviors, Tehran University of Medical Sciences, Tehran, Iran.

[4] Translational Ophthalmology Research Center, Farabi Eye Hospital, Tehran University of Medical Sciences, Tehran, Iran.

[5] Department of Ophthalmology, University of Padova, Padova, Italy.

[6] IRCCS Fondazione Bietti, Roma, Italy.

Disclosure(s):

All authors have completed and submitted the ICMJE disclosures form.

The authors made the following disclosures:

E.M.: Scientific Supervisor − Ophthal software.

F.B.: Consultant − Allergan Inc (Irvine, California, USA), Bayer Shering-Pharma (Berlin, Germany), Hoffmann-La-Roche (Basel, Switzerland), Novartis (Basel, Switzerland), Sanofi-Aventis (Paris, France), Thrombogenics (Heverlee, Belgium), Zeiss (Dublin, USA), Boehringer-Ingelheim, Fidia Sooft, Ntc Pharma, and Sifi.

The Ophthal software was developed with the unconditional support of AbbVie Srl.

Support for Open Access publication was provided by IRCCS San Raffaele Scientific Institute.

HUMAN SUBJECTS: Human subjects were included in this study. The Ospedale San Raffaele institutional review board approved the study. All research adhered to the tenets of the Declaration of Helsinki. Written informed consent was waived by the local institutional review board due to the retrospective design of the study.

No animal subjects were used in this study.

Author Contributions:

Conception and design: Cicinelli

Data collection: Cicinelli, Leonardo, Maiucci, Martino, Ziafati, Bousyf, Lattanzio

Analysis and interpretation: Cicinelli, Leonardo, Maiucci, Martino, Ziafati, Frizziero, Lattanzio, Midena, Bandello

Obtained funding: N/A

Overall responsibility: Cicinelli, Leonardo, Maiucci, Martino, Ziafati, Bousyf, Frizziero, Lattanzio, Midena, Bandello

Abbreviations and Acronyms:
AI = artificial intelligence; **BRB** = blood-retinal barrier; **CI** = confidence interval; **CST** = central subfield thickness; **DEX** = dexamethasone; **DME** = diabetic macular edema; **DR** = diabetic retinopathy; **DRIL** = disorganization of the retinal inner layers; **ELM** = external limiting membrane; **EZ** = ellipsoid zone; **HRF** = hyperreflective foci; **IRF** = intraretinal fluid; **IVTA** = intravitreal triamcinolone acetonide; **LogMAR** = logarithm of the minimum angle of resolution; **SD** = standard deviation; **SD-OCT** = spectral-domain; **OCT SRF** = subretinal fluid; **VA** = visual acuity.

Keywords:
AI, Anti-VEGF, Artificial intelligence, Dexamethasone implant, Diabetic macular edema.

Correspondence:
Maria Vittoria Cicinelli, MD, Department of Ophthalmology, IRCCS San Raffaele Scientific Institute, Via Olgettina 60, Milan 20132, Italy. E-mail: Cicinelli.mariavittoria@hsr.it.

References

1. Starace V, Battista M, Brambati M, et al. The role of inflammation and neurodegeneration in diabetic macular edema. *Ther Adv Ophthalmol*. 2021;13:25158414211055963.
2. Bressler NM, Beaulieu WT, Glassman AR, et al. Persistent macular thickening following intravitreous aflibercept, bevacizumab, or ranibizumab for central-involved diabetic macular edema with vision impairment: a secondary analysis of a randomized clinical trial. *JAMA Ophthalmol*. 2018;136:257–269.
3. Cicinelli MV, Rabiolo A, Capone L, et al. Factors associated with the response to fluocinolone acetonide 0.19 mg in diabetic macular oedema evaluated as the area-under-the-curve. *Eye (Lond)*. 2023;37:242–248.
4. Zur D, Iglicki M, Busch C, et al. OCT biomarkers as functional outcome predictors in diabetic macular edema treated with dexamethasone implant. *Ophthalmology*. 2018;125:267–275.
5. Schmidt-Erfurth U, Reiter GS, Riedl S, et al. AI-based monitoring of retinal fluid in disease activity and under therapy. *Prog Retin Eye Res*. 2022;86:100972.
6. Roberts PK, Vogl WD, Gerendas BS, et al. Quantification of fluid resolution and visual acuity gain in patients with diabetic macular edema using deep learning: a post hoc analysis of a randomized clinical trial. *JAMA Ophthalmol*. 2020;138:945–953.
7. Vujosevic S, Torresin T, Berton M, et al. Diabetic macular edema with and without subfoveal neuroretinal detachment: two different morphologic and functional entities. *Am J Ophthalmol*. 2017;181:149–155.
8. Midena E, Pilotto E, Bini S. Hyperreflective intraretinal foci as an OCT biomarker of retinal inflammation in diabetic macular edema. *Invest Ophthalmol Vis Sci*. 2018;59:5366.
9. Munk MR, Somfai GM, de Smet MD, et al. The role of intravitreal corticosteroids in the treatment of DME: predictive OCT biomarkers. *Int J Mol Sci*. 2022;23:7585.
10. Sinha P, Calfee CS, Delucchi KL. Practitioner's guide to latent class analysis: methodological considerations and common pitfalls. *Crit Care Med*. 2021;49:e63–e79.
11. Midena E, Toto L, Frizziero L, et al. Validation of an automated artificial intelligence algorithm for the quantification of major OCT parameters in diabetic macular edema. *J Clin Med*. 2023;12:2134.
12. Scrucca C LF, Murphy TB, Raftery AE. *Model-Based Clustering, Classification, and Density Estimation Using mclust in R*. Boca Raton, FL: Chapman and Hall/CRC; 2023.
13. Michl M, Fabianska M, Seebock P, et al. Automated quantification of macular fluid in retinal diseases and their response to anti-VEGF therapy. *Br J Ophthalmol*. 2022;106:113–120.
14. Qaum T, Xu Q, Joussen AM, et al. VEGF-initiated blood-retinal barrier breakdown in early diabetes. *Invest Ophthalmol Vis Sci*. 2001;42:2408–2413.
15. Hammes HP, Lin J, Renner O, et al. Pericytes and the pathogenesis of diabetic retinopathy. *Diabetes*. 2002;51:3107–3112.
16. Bringmann A, Pannicke T, Grosche J, et al. Muller cells in the healthy and diseased retina. *Prog Retin Eye Res*. 2006;25:397–424.
17. Lai D, Wu Y, Shao C, Qiu Q. The role of muller cells in diabetic macular edema. *Invest Ophthalmol Vis Sci*. 2023;64:8.
18. Wong TY, Haskova Z, Asik K, et al. Faricimab treat-and-extend for diabetic macular edema: two-year results from the randomized phase 3 YOSEMITE and RHINE trials. *Ophthalmology*. 2024;131:708–723.
19. Cicinelli MV, Cavalleri M, Querques L, et al. Early response to ranibizumab predictive of functional outcome after dexamethasone for unresponsive diabetic macular oedema. *Br J Ophthalmol*. 2017;101:1689–1693.
20. Busch C, Zur D, Fraser-Bell S, et al. Shall we stay, or shall we switch? Continued anti-VEGF therapy versus early switch to dexamethasone implant in refractory diabetic macular edema. *Acta Diabetol*. 2018;55:789–796.
21. Pawloff M, Bogunovic H, Gruber A, et al. Systematic correlation of central subfield thickness with retinal fluid volumes quantified by deep learning in the major exudative macular diseases. *Retina*. 2022;42:831–841.
22. Deak GG, Schmidt-Erfurth UM, Jampol LM. Correlation of central retinal thickness and visual acuity in diabetic macular edema. *JAMA Ophthalmol*. 2018;136:1215–1216.
23. Panozzo G, Cicinelli MV, Dalla MG, et al. Enhancing diabetic macular edema treatment outcomes: exploring the ESASO classification and structural OCT biomarkers. *Ophthalmol Ther*. 2024;13:1383–1398.
24. Cicinelli MV, Gerosolima C, Scandale P, et al. Clinical and imaging biomarkers of response to intravitreal dexamethasone implant in eyes with non-infectious uveitic macular oedema. *Eye (Lond)*. 2024;38:910–916.
25. Wirth MA, Wons J, Freiberg FJ, et al. Impact of long-term intravitreal anti-vascular endothelial growth factor on preexisting microstructural alterations in diabetic macular edema. *Retina*. 2018;38:1824–1829.
26. Gerendas BS, Prager S, Deak G, et al. Predictive imaging biomarkers relevant for functional and anatomical outcomes during ranibizumab therapy of diabetic macular oedema. *Br J Ophthalmol*. 2018;102:195–203.
27. Panozzo G, Cicinelli MV, Augustin AJ, et al. An optical coherence tomography-based grading of diabetic maculopathy proposed by an international expert panel: the European school for advanced studies in ophthalmology classification. *Eur J Ophthalmol*. 2020;30:8–18.
28. Shimura M, Yasuda K, Nakazawa T, et al. Visual outcome after intravitreal triamcinolone acetonide depends on optical coherence tomographic patterns in patients with diffuse diabetic macular edema. *Retina*. 2011;31:748–754.
29. Yanoff M, Fine BS, Brucker AJ, Eagle Jr RC. Pathology of human cystoid macular edema. *Surv Ophthalmol*. 1984;28(Suppl):505–511.
30. Tsai WS, Thottarath S, Gurudas S, et al. Characterization of the structural and functional alteration in eyes with diabetic macular ischemia. *Ophthalmol Retina*. 2023;7:142–152.
31. Lee H, Kang KE, Chung H, Kim HC. Three-dimensional analysis of morphologic changes and visual outcomes in diabetic macular edema. *Jpn J Ophthalmol*. 2019;63:234–242.
32. Keenan TDL, Chakravarthy U, Loewenstein A, et al. Automated quantitative assessment of retinal fluid volumes as important biomarkers in neovascular age-related macular degeneration. *Am J Ophthalmol*. 2021;224:267–281.